Discrete Boltzmann trans-scale modeling of high-speed compressible flows

Yanbiao Gan,[1,2] Aiguo Xu,[3,4,*] Guangcai Zhang,[3] Yudong Zhang,[3,5] and Sauro Succi[6,7]

[1]*North China Institute of Aerospace Engineering, Langfang 065000, China*

[2]*College of Mathematics and Informatics & FJKLMAA, Fujian Normal University, Fuzhou 350007, China*

[3]*National Key Laboratory of Computational Physics, Institute of Applied Physics and Computational Mathematics, P.O. Box 8009-26, Beijing 100088, China*

[4]*Center for Applied Physics and Technology, MOE Key Center for High Energy Density Physics Simulations, College of Engineering, Peking University, Beijing 100871, China*

[5]*Key Laboratory of Transient Physics, Nanjing University of Science and Technology, Nanjing 210094, China*

[6]*Center for Life Nano Science at La Sapienza, Fondazione Istituto Italiano di Tecnologia, Viale Regina Margherita 295, 00161 Roma, Italy*

[7]*Physics Department and Institute for Applied Computational Science, John A. Paulson School of Applied Science and Engineering, Harvard University, Oxford Street 29, Cambridge, Massachusetts 02138, USA*

(Received 13 January 2018; revised manuscript received 19 April 2018; published 31 May 2018)

We present a general framework for constructing trans-scale *discrete Boltzmann models* (DBMs) for high-speed compressible flows ranging from continuum to transition regime. This is achieved by designing a higher-order discrete equilibrium distribution function that satisfies additional nonhydrodynamic kinetic moments. To characterize the *thermodynamic nonequilibrium* (TNE) effects and estimate the condition under which the DBMs at various levels should be used, two measures are presented: (i) the relative TNE strength, describing the relative strength of the $(N+1)$th order TNE effects to the Nth order one; (ii) the TNE discrepancy between DBM simulation and relevant theoretical analysis. Whether or not the higher-order TNE effects should be taken into account in the modeling and which level of DBM should be adopted is best described by the relative TNE intensity and/or the discrepancy rather than by the value of the Knudsen number. As a model example, a two-dimensional DBM with 26 discrete velocities at Burnett level is formulated, verified, and validated.

DOI: 10.1103/PhysRevE.97.053312

I. INTRODUCTION

High-speed compressible flows with substantial *hydrodynamic and thermodynamic nonequilibrium* (HNE and TNE, respectively) effects are ubiquitous in nature, high pressure science and technology [1], turbulent combustion [2], shock wave therapy [3,4], food processing [5], hypersonic flows associated with spacecraft reentry into the upper atmosphere [6–9], strong shock waves in the inertial confinement fusion process [10,11], etc. More specifically, in the last two representative fields, both rarefied gas flows at high altitude and limited shock wave thickness (typically of the order of a few mean-free-paths of molecules, characterized by drastic changes in state variables) give rise to high Knudsen number and significant out-of-equilibrium scenarios. Additionally, most hypersonic vehicles operate over a wide range of Knudsen number in different parts of the equipment, simultaneously [6–9,12]. Consequently, various flow regimes with totally different aerothermodynamics, ranging from continuum, slip, transition, even to free molecular flow regimes coexist in the entire flow, which adds considerably to the complexity of the problem. For such complex nonequilibrium systems, the appropriateness of constitutive relations, which are associated with the TNE effects, ultimately determines the accuracy of the hydrodynamic model. Besides the HNE effects described by the hydrodynamic model, the evolution of TNE characteristics helps to dynamically characterize the nonequilibrium state and understand the constitutive relations. Therefore, establishing a physically accurate and computationally efficient predictive model to investigate these extremely complex HNE and TNE behaviors is of both great academic significance and industrial practical value. Undoubtedly, it is a long-standing challenge.

The difficulty arises from the fact that various temporal and spatial scales are associated and coupled with distinct physics. Consequently, the flow lacks scale separation and the complexity springs up [13]. Continuum-based Navier-Stokes (NS) equations, even with slip boundary conditions, are not adequate to describe these kinds of flows. The inadequacy stems from the linear constitutive relations for viscous stress and heat flux assumed in the NS model, which are no longer valid for the far-from-equilibrium system. Thus, it is reasonable to conjecture that the inclusion of higher-order terms in the constitutive relations can improve the multiscale predictive capability of such continuum models. Along this line, the Burnett-like equations, which are expected to perform well in the continuum-transition regime, are obtained from the CE expansion of Boltzmann equation. Nevertheless, the extended hydrodynamic models are still subject to at least the following four constraints that greatly hamper their wide applications: (i) small wavelength instability as the grids are refined; (ii) necessity of additional boundary conditions, (iii) complicated programming owing to the existence of extraordinarily complex and numerous higher-order derivatives, and

*Corresponding author: xu_aiguo@iapcm.ac.cn

(iv) the evolution equations of relevant higher-order nonconservative kinetic moments are not included, even though they are needed for an exact characterization of the nonequilibrium behaviors and understanding the kinetic mechanisms for the nonlinear constitutive relations. Currently, the particle-based direct simulation Monte Carlo (DSMC) method has been regarded as a reliable and accurate approach for simulating rarefied gas flows with high-speed and high Knudsen number [14–16]. Unfortunately, it becomes extremely time-consuming and prohibitively memory-demanding for simulating nearly continuum flows where intensive particle collisions take place due to the limitation to the cell size and time step which are, respectively, less than the mean-free-path and particle collision time. So, it still cannot be qualified as a computationally efficient candidate for modeling flows in the continuum-transition regime.

Being one of the most fundamental equations of the nonequilibrium statistical physics, the Boltzmann equation is capable of handling thermohydrodynamics for the full spectrum of flow regimes. However, the direct solution of the full Boltzmann equation encounters serious difficulties due to the inherent nonlinearity, multidimensionality, together with the multiple integrodifferential nature of the collision term. Therefore, developing approximate and simplified kinetic models that can preserve the most relevant features of the Boltzmann equation is currently an important and essential attempt [6–8,17–23]. Examples in this class are the discrete ordinate method [6–8,24], the unified gas kinetic scheme (UGKS) and the discrete UGKS [25–32], the regularized 13 (26) moment approach [33–37], the quadrature method of moments [38–40], the lattice Boltzmann kinetic method (LBKM) [41–59], or discrete Boltzmann method/model (DBM) [60–67]. In this paper, we focus only on the strategies for constructing higher-order LBKM/DBM beyond NS hydrodynamics [68–85], that can be roughly classified into the following five categories, i.e., the Hermite expansion approach, the elaborate boundary condition way, the effective local mean-free-path approach, the coupled particle-continuum scheme, and the collisional lattice Boltzmann approach. The Hermite expansion approach, presented by Shan *et al.* [77–79], is a straightforward and systematic framework for constructing higher-order LB approximations to the Boltzmann-BGK equation beyond the NS level by using high-order Hermite expansions with appropriate quadratures. In this way, the order of Hermite expansion is responsible for obtaining correct kinetic moment relations. Hence, through incorporating higher-order terms in the Hermite expansions, hydrodynamic models at various levels can be obtained at any order of truncation of the Hermite polynomials. To capture the velocity-slip and temperature-jump phenomena in the slip regime, an alternative way is to design elaborate boundary conditions [80–83], for instance, the bounce back, specular reflection, diffuse-reflection, and Maxwell-type boundary conditions, etc. In the third approach, Zhang *et al.* [84,85] proposed a novel wall function to modify the local mean-free-path and the relaxation time through which to take into account the nonequilibrium characteristics in the Knudsen layer. This simple treatment is effective for Knudsen numbers up to 1.58. The fourth approach [75,76] consists of two coupled elements: the DSMC and LBKM which work not only for the weak nonequiulbrium regions but also the strong nonequilibrium regions. The delicate combination actually acts as an efficient multiscale strategy with respect to the full DSMC. The last approach was presented by Green *et al.* [59], the main difference between their method and the conventional LBKM is the consideration of the detailed effects of collisional interactions via the full collision operator of the Boltzmann equation without any equilibrium based approximations. Such a treatment makes the method particularly suitable for simulating highly nonequilibrium flows with relative large Knudsen number, although it involves a greater computational load due to the numerical solution of a system of coupled, nonlinear ordinary differential equations when dealing with the fivefold Boltzmann collision integral. Nevertheless, it should be noted that all the above-mentioned attempts are suitable for isothermal or thermal case with sufficiently small Mach number. Significant effort is still urgently required to develop robust high-order LBKM/DBM for modeling highly nonequilibrium flows with high Mach number and significant thermal effects.

To this end, we resort to DBM, which aims to probe the trans- and supercritical fluid behaviors [60] or to study simultaneously the HNE and TNE behaviors, and has brought significant new physical insights into the systems [54,55,61–67,86,87]. Concretely, in this paper, we present a general framework for developing trans-scale DBMs for high-speed compressible flows ranging from continuum to transition regime through the construction of higher-order discrete equilibrium distribution function (DEDF) that satisfies additional higher-order kinetic moments and the design of higher-order isotropic discrete-velocity model (DVM) with smaller number of discrete velocities; as a model example, we present a two-dimensional compressible DBM with 26 discrete velocities at the Burnett level; determine the relations between macroscopic dissipations and nonequilibrium measures defined through DBM, and provide a more general constitutive relations for viscous stress and heat flux that can be used to improve macroscopic modeling.

II. HIGHER-ORDER DBM AND HIGHER-ORDER CONSTITUTIVE RELATIONS

The key step of physical modeling of complex fluid system is the coarse-graining process. The principle for such a simplification process is that the physical quantities we choose to measure the system should stay unchanged after simplification. On the whole, the discrete Boltzmann trans-scale modeling procedure includes the following four steps, as shown in Fig. 1: (I) linearization of the collision term; (II) discretization of the particle velocity space; (III) determination of the required kinetic moments via Chapman-Enskog (CE) analysis; (IV) acquisition of the DEDF and DVM according to the required kinetic moments.

Next, we explain what we really imply and what we conduct in each step. In step (I), it is well known that the original collision term of the Boltzmann equation $J(f, f^*)$ is too complex to be solved directly, where f and f^* are distribution functions before and after collisions, respectively. The simplest way to linearize it is to introduce a local equilibrium distribution function $f^{(0)}$ and write the collision term into the BGK-like form [88] $J = -\frac{1}{\tau}[f - f^{(0)}]$, where

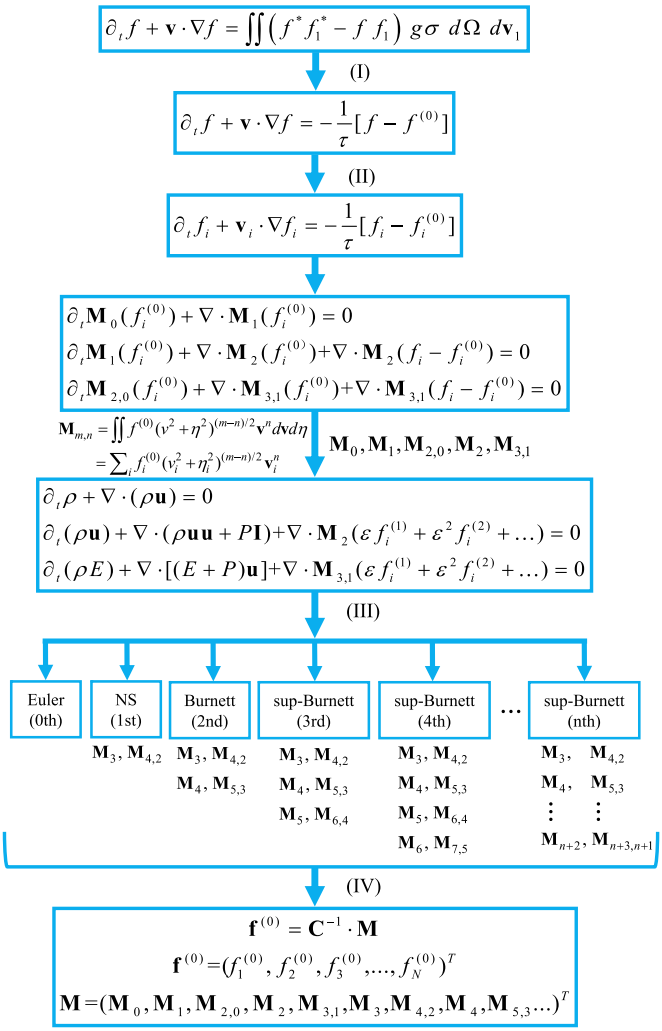

FIG. 1. Flow chart for the discrete Boltzmann trans-scale modeling of compressible flows.

$f^{(0)} = \frac{\rho}{2\pi RT}\left(\frac{1}{2\pi nRT}\right)^{1/2}\exp\left[-\frac{(\mathbf{v}-\mathbf{u})^2}{2RT} - \frac{\eta^2}{2nRT}\right]$ is the Maxwellian distribution function, where ρ, $\mathbf{v}$, $\mathbf{u}$, and T are the local density, particle velocity, flow velocity, and temperature, respectively. R is the gas constant, η is a free parameter introduced to describe the n extra degrees of freedom corresponding to molecular rotation and/or vibration. Owing to its simplicity, the BGK approximation is the most extensively used. Besides this, other models, including the ellipsoidal statistical BGK model [89], Shakhov model [90], Rykov model [91], Liu model [92], etc., have also been used to simplify the full collision operator of the Boltzmann equation and to tune the Prandtl number.

To perform simulation, we have to write the BGK-like Boltzmann equation in a discrete form, i.e., the discrete Boltzmann equation,

$$\partial_t f_i + \mathbf{v}_i\cdot\nabla f_i = -\frac{1}{\tau}\left[f_i - f_i^{(0)}\right], \tag{1}$$

which results in step (II). The discretization of six-dimensional phase-space, i.e., position-and-velocity space, is however prohibitively expensive from the computational standpoint. To find an effective way to discretize the particle velocity space, we go back to consider what we really need and at which level the hydrodynamic equations are recovered from the discrete Boltzmann equation. In fact, in the DB modeling, we do not expect to describe the system by using specific values of the discrete distribution function f_i, but rather the kinetic moments of f_i. The CE analysis informs us that the calculations of all the kinetic moments of f_i can finally resort to those of the DEDF $f_i^{(0)}$. Therefore, we should ensure that these kinetic moments of $f^{(0)}$, originally in integral form, can be calculated in summation form during the modeling process.

To determine which level the hydrodynamic equations are recovered and which kinetic moments of $f_i^{(0)}$ are needed, one can derive the hydrodynamic equations from the discrete Boltzmann equation via CE multiscale expansion. Essentially, the derivation of hydrodynamic equations from discrete Boltzmann equation is sufficient but not necessary. Compared with the traditional modeling schemes based on continuum assumption, DBM is a kind of different scheme to model the nonequilibrium flows. DBM modeling and simulation do not need the hydrodynamic equations; one needs only to determine the required kinetic moments via CE procedure, which is one of the prominent advantages of DBM and the key point of the manuscript. Then we show the derivation from discrete Boltzmann equation to hydrodynamic equations, which serves the purpose of showing why such a modeling scheme does work.

It is found that, when $f_i^{(0)}$ satisfies the following five kinetic moments,

$$\mathbf{M}_0 = \sum_i f_i^{(0)} = \rho, \tag{2}$$

$$\mathbf{M}_1 = \sum_i f_i^{(0)}\mathbf{v}_i = \rho\mathbf{u}, \tag{3}$$

$$\mathbf{M}_{2,0} = \sum_i \frac{1}{2} f_i^{(0)}\left(v_i^2 + \eta_i^2\right) = \frac{1}{2}\rho[(n+2)RT + u^2], \tag{4}$$

$$\mathbf{M}_2 = \sum_i f_i^{(0)}\mathbf{v}_i\mathbf{v}_i = \rho(RT\mathbf{I} + \mathbf{u}\mathbf{u}), \tag{5}$$

$$\mathbf{M}_{3,1} = \sum_i \frac{1}{2} f_i^{(0)}\left(v_i^2 + \eta_i^2\right)\mathbf{v}_i = \frac{1}{2}\rho\mathbf{u}[(n+4)RT + u^2], \tag{6}$$

taking moments of Eq. (1) with the collision invariant vector $1, \mathbf{v}_i, \frac{1}{2}(\mathbf{v}_i^2 + \eta_i^2)$, gives rise to the following generalized set of thermohydrodynamic equations,

$$\partial_t\rho + \nabla\cdot(\rho\mathbf{u}) = 0, \tag{7}$$

$$\partial_t(\rho\mathbf{u}) + \nabla\cdot(\rho\mathbf{u}\mathbf{u} + P\mathbf{I} + \mathbf{\Delta}_2^*) = 0, \tag{8}$$

$$\partial_t(\rho E) + \nabla\cdot[(E+P)\mathbf{u} + \mathbf{\Delta}_2^*\cdot\mathbf{u} + \mathbf{\Delta}_{3,1}^*] = 0, \tag{9}$$

where $P = \rho RT$ is the local hydrostatic pressure and $E = c_v T + u^2/2$ the total energy with $c_v = (n+2)R/2$ the specific heat at constant volume. Here "satisfaction" means the moments calculated from the summation of $f_i^{(0)}$ should be the same as those from the integration of $f^{(0)}$,

$$\sum_i f_i^{(0)}\Psi(\mathbf{v}_i, \eta_i) = \mathbf{M}_{m,n} = \iint f^{(0)}\Psi(\mathbf{v}, \eta)d\mathbf{v}d\eta, \tag{10}$$

where $\Psi(\mathbf{v}_i,\eta_i)=[1,\mathbf{v}_i,\frac{1}{2}(v_i^2+\eta_i^2),\mathbf{v}_i\mathbf{v}_i,\frac{1}{2}(v_i^2+\eta_i^2)\mathbf{v}_i]^T$. Note that Eqs. (8) and (9) are unclosed. To close these equations at various levels, we should deduce the explicit expressions for the TNE measures $\mathbf{\Delta}_2^*$ and $\mathbf{\Delta}_{3,1}^*$. Physically, these two measures reflect molecular individualism on top of organized collective motion, which are conventionally labeled as *nonorganized moment fluxes* (NOMF),

$$\mathbf{\Delta}_2^*=\mathbf{M}_2^*\big(f_i-f_i^{(0)}\big)=\sum_i\big(f_i-f_i^{(0)}\big)\mathbf{v}_i^*\mathbf{v}_i^*, \tag{11}$$

and *nonorganized energy fluxes* (NOEF),

$$\mathbf{\Delta}_{3,1}^*=\mathbf{M}_{3,1}^*\big(f_i-f_i^{(0)}\big)=\sum_i\big(f_i-f_i^{(0)}\big)\frac{v_i^{*2}+\eta_i^2}{2}\mathbf{v}_i^*, \tag{12}$$

respectively. $\mathbf{M}_2^*$ and $\mathbf{M}_{3,1}^*$ are kinetic central moments. Compared with NS and Burnett equations, $\mathbf{\Delta}_2^*$ ($\mathbf{\Delta}_{3,1}^*$) corresponds to the full viscous stress tensor $\boldsymbol{\sigma}$ (heat flux $\mathbf{j}_q$). Therefore, the relation between TNE measure and macroscopic dissipation is clarified. Of course, the derivations of $\mathbf{\Delta}_2^*$ and $\mathbf{\Delta}_{3,1}^*$ will induce additional requirements on moments of $f_i^{(0)}$.

Step (III) demonstrates that to recover hydrodynamic equations at different levels, $f_i^{(0)}$ should satisfy different additional kinetic moments. The requirements on kinetic moments of $f_i^{(0)}$ can be determined as follows. To perform the CE expansion on both sides of Eq. (1), we first introduce expansions

$$f_i=f_i^{(0)}+\epsilon f_i^{(1)}+\epsilon^2 f_i^{(2)}+\cdots, \tag{13}$$

$$\partial_t=\epsilon\partial_{t_1}+\epsilon^2\partial_{t_2}+\cdots, \tag{14}$$

$$\nabla=\epsilon\nabla_1, \tag{15}$$

where $\epsilon^j f_i^{(j)}$ is the jth order departure from $f_i^{(0)}$ in Knudsen number ϵ, and $\epsilon^j\partial_{t_j}$ is jth order term in ϵ. Substituting Eqs. (13)–(15) into Eq. (1) and equating terms that have the same orders in ϵ gives the following formulations for $f_i^{(1)}$ and $f_i^{(2)}$:

$$\epsilon f_i^{(1)}=-\tau\big[\epsilon\partial_{t_1}f_i^{(0)}+\epsilon\nabla_1\cdot\big(f_i^{(0)}\mathbf{v}_i\big)\big], \tag{16}$$

and

$$\begin{aligned}\epsilon^2 f_i^{(2)}&=-\tau\big[\epsilon^2\partial_{t_2}f_i^{(0)}+\epsilon\partial_{t_1}\big(\epsilon f_i^{(1)}\big)+\epsilon\nabla_1\cdot\big(\epsilon f_i^{(1)}\mathbf{v}_i\big)\big]\\&=-\tau\epsilon^2\partial_{t_2}f_i^{(0)}+\tau^2\epsilon^2\partial_{t_1}^2f_i^{(0)}+\tau^2\epsilon^2\partial_{t_1}\big[\nabla_1\cdot\big(f_i^{(0)}\mathbf{v}_i\big)\big]\\&\quad+\tau^2\epsilon^2\nabla_1\cdot\big[\partial_{t_1}f_i^{(0)}\mathbf{v}_i+\nabla_1\cdot\big(f_i^{(0)}\mathbf{v}_i\mathbf{v}_i\big)\big].\end{aligned} \tag{17}$$

It is clear that (i) $\epsilon f_i^{(1)}$ and $\epsilon^2 f_i^{(2)}$ can be expressed as formulations of $f_i^{(0)}$; (ii) $\epsilon f_i^{(1)}$ includes a polynomial of $\mathbf{v}_i$ of one order higher than that in $f_i^{(0)}$; (iii) $\epsilon^2 f_i^{(2)}$ includes a polynomial of $\mathbf{v}_i$ of one order higher than that in $\epsilon f_i^{(1)}$ but two orders higher than that in $f_i^{(0)}$. Obviously, to achieve explicit expressions for the first-order constitutive relations, $\mathbf{\Delta}_2^{(1)*}=\sum_i\epsilon f_i^{(1)}\mathbf{v}_i^*\mathbf{v}_i^*$ and $\mathbf{\Delta}_{3,1}^{(1)*}=\sum_i\epsilon f_i^{(1)}\frac{v_i^{*2}+\eta_i^2}{2}\mathbf{v}_i^*$, the highest order nonequilibrium kinetic moments that $f_i^{(0)}$ should further satisfy are

$$\mathbf{M}_3=\sum_i f_i^{(0)}\mathbf{v}_i\mathbf{v}_i\mathbf{v}_i=\rho(RT\mathbf{\Theta}+\mathbf{uuu}), \tag{18}$$

$$\begin{aligned}\mathbf{M}_{4,2}=\sum_i f_i^{(0)}\frac{v_i^2+\eta_i^2}{2}\mathbf{v}_i\mathbf{v}_i&=\rho\bigg[\bigg(\frac{n+4}{2}RT+\frac{u^2}{2}\bigg)RT\mathbf{I}\\&\quad+\bigg(\frac{n+6}{2}RT+\frac{u^2}{2}\bigg)\mathbf{uu}\bigg],\end{aligned} \tag{19}$$

respectively. Similarly, to achieve explicit expressions for the second-order constitutive relations, $f_i^{(0)}$ should satisfy $\mathbf{M}_4$ and $\mathbf{M}_{5,3}$,

$$\mathbf{M}_4=\sum_i f_i^{(0)}\mathbf{v}_i\mathbf{v}_i\mathbf{v}_i\mathbf{v}_i=\rho(R^2T^2\mathbf{\Pi}+RT\,\mathbf{\Xi}+\mathbf{uuuu}), \tag{20}$$

$$\begin{aligned}\mathbf{M}_{5,3}&=\sum_i\frac{1}{2}f_i^{(0)}\big(v_i^2+\eta_i^2\big)\mathbf{v}_i\mathbf{v}_i\mathbf{v}_i\\&=\rho\bigg[\bigg(\frac{n+8}{2}RT+\frac{u^2}{2}\bigg)\mathbf{uuu}\\&\quad+\bigg(\frac{n+6}{2}RT+\frac{u^2}{2}\bigg)RT\mathbf{\Theta}\bigg],\end{aligned} \tag{21}$$

with $\mathbf{\Theta}=(u_\alpha\delta_{\beta\gamma}+u_\beta\delta_{\alpha\gamma}+u_\gamma\delta_{\alpha\beta})\widehat{\mathbf{e}}_\alpha\widehat{\mathbf{e}}_\beta\widehat{\mathbf{e}}_\gamma$, $\mathbf{\Pi}=(\delta_{\alpha\beta}\delta_{\gamma\lambda}+\delta_{\alpha\gamma}\delta_{\beta\lambda}+\delta_{\alpha\lambda}\delta_{\beta\gamma})\widehat{\mathbf{e}}_\alpha\widehat{\mathbf{e}}_\beta\widehat{\mathbf{e}}_\gamma\widehat{\mathbf{e}}_\lambda$, $\mathbf{\Xi}=(u_\alpha u_\beta\delta_{\gamma\lambda}+u_\alpha u_\gamma\delta_{\beta\lambda}+u_\alpha u_\lambda\delta_{\beta\gamma}+u_\beta u_\gamma\delta_{\alpha\lambda}+u_\beta u_\lambda\delta_{\alpha\gamma}+u_\gamma u_\lambda\delta_{\alpha\beta})\widehat{\mathbf{e}}_\alpha\widehat{\mathbf{e}}_\beta\widehat{\mathbf{e}}_\gamma\widehat{\mathbf{e}}_\lambda$, and $(\widehat{\mathbf{e}}_\alpha,\widehat{\mathbf{e}}_\beta,\widehat{\mathbf{e}}_\gamma,\widehat{\mathbf{e}}_\lambda)$ denoting unit vectors along the α, β, γ, and λ axes, respectively, of a fixed coordinate system.

By using the above needed kinetic moments and after some tedious but straightforward algebraic manipulation, we acquire relations between thermodynamic forces and fluxes,

$$\mathbf{\Delta}_2^{*(1)}=-\mu\bigg[\nabla\mathbf{u}+(\nabla\mathbf{u})^T-\frac{2}{n+2}\mathbf{I}\nabla\cdot\mathbf{u}\bigg]=-\boldsymbol{\sigma}_{\rm NS}, \tag{22}$$

$$\mathbf{\Delta}_{3,1}^{*(1)}=-\kappa\nabla T=-\mathbf{j}_{q,\rm NS}, \tag{23}$$

where the first-order NOMF and NOEF are just the negative viscous stress tensor and heat flux at the NS level, with $\mu=P\tau$, $\kappa=c_pP\tau$ are viscosity coefficient and heat conductivity, respectively. Here $c_p=(n+4)R/2$ is the specific heat at constant pressure. Expressions for the second-order constitutive relations $\mathbf{\Delta}_2^{*(2)}=\sum_i\epsilon^2 f_i^{(2)}\mathbf{v}_i^*\mathbf{v}_i^*=-(\boldsymbol{\sigma}_{\rm Burnett}-\boldsymbol{\sigma}_{\rm NS})$ and $\mathbf{\Delta}_{3,1}^{*(2)}=\sum_i\epsilon^2 f_i^{(2)}\frac{v_i^{*2}+\eta_i^2}{2}\mathbf{v}_i^*=-(\mathbf{j}_{q,\,\rm Burnett}-\mathbf{j}_{q,\rm NS})$, which are displayed in the Appendix. So far, the higher-order constitutive relations for viscous stress and heat transfer at the Burnett level have been given by $\mathbf{\Delta}_2^*=\mathbf{\Delta}_2^{*(1)}+\mathbf{\Delta}_2^{*(2)}$ and $\mathbf{\Delta}_{3,1}^*=\mathbf{\Delta}_{3,1}^{*(1)}+\mathbf{\Delta}_{3,1}^{*(2)}$, which are expected to noticeably improve the macroscopic modeling. Counterparts at super-Burnett levels can be deduced in a similar way.

Finally, in step (IV), we obtain the analytical expression for DEDF via inversely solving the required kinetic moments. Details are as follows. In the two-dimensional case, the above moments $\mathbf{M}_0$, $\mathbf{M}_1$, $\mathbf{M}_{2,0}$, $\mathbf{M}_2$, $\mathbf{M}_{3,1}$, $\mathbf{M}_3$, $\mathbf{M}_{4,2}$, $\mathbf{M}_4$, and $\mathbf{M}_{5,3}$ have 25 components. For physical symmetry and numerical

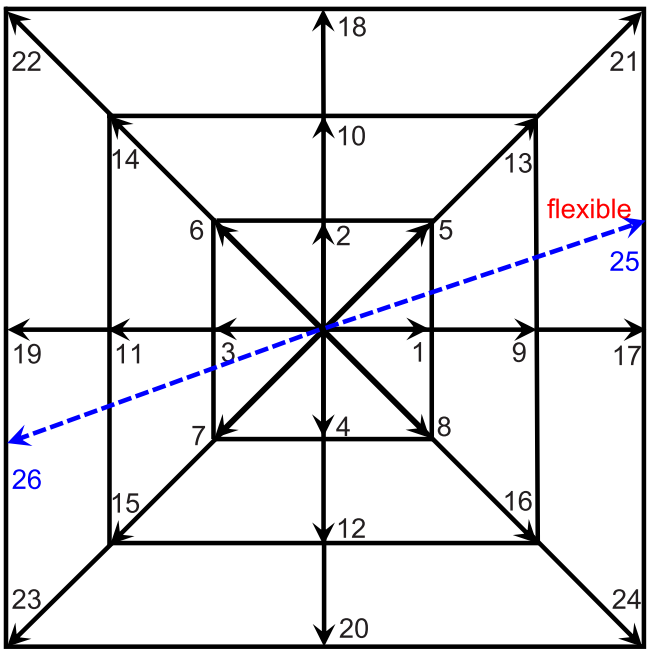

FIG. 2. Schematic of the D2V26 discrete-velocity model, where $\mathbf{v}_{25}(=-\mathbf{v}_{26})$ is a flexible vector, adjusted to guarantee the existence of $\mathbf{C}^{-1}$.

stability, we add the following one:

$$\mathbf{M}_{4,0} = \sum_i \frac{1}{2} f_i^{(0)} \left(v_i^2 + \eta_i^2\right)^2 = \rho\left[\frac{3n^2+4n+8}{2} R^2T^2 + (n+4)RTu^2 + \frac{u^4}{2}\right]. \quad (24)$$

These moments can be rewritten in a matrix form,

$$\mathbf{C}\cdot\mathbf{f}^{(0)} = \mathbf{M}, \quad (25)$$

where $\mathbf{f}^{(0)} = (f_1^{(0)}, f_2^{(0)}, \ldots, f_{26}^{(0)})^T$, $\mathbf{M} = (M_1, M_2, \ldots, M_{26})^T = (M_0, M_{1x}, M_{1y}, \ldots, M_{4,0})^T$ is the set of moments of $f_i^{(0)}$. $\mathbf{C} = (\mathbf{c}_1, \mathbf{c}_2, \ldots, \mathbf{c}_{26})$ is a 26×26 matrix bridging the DEDF and the kinetic moments with $\mathbf{c}_i = (1, v_{ix}, v_{iy}, \ldots, \frac{1}{2}(\mathbf{v}_i^2 + \eta_i^2)^2)^T$. As a result, $\mathbf{f}^{(0)}$ can be calculated in the following way [53],

$$\mathbf{f}^{(0)} = \mathbf{C}^{-1}\cdot\mathbf{M}, \quad (26)$$

where $\mathbf{C}^{-1}$ is the inverse of matrix $\mathbf{C}$. A two-dimensional DVM with 26 discrete velocities, schematically drawn in Fig. 2, is appropriately designed to discretize the velocity space and to ensure the existence of $\mathbf{C}^{-1}$,

$$(v_{ix}, v_{iy}) = \begin{cases} \text{cyc} : c(\pm1,0) & \text{for } 1 \leqslant i \leqslant 4 \\ c(\pm1, \pm1) & \text{for } 5 \leqslant i \leqslant 8 \\ \text{cyc} : 2c(\pm1,0) & \text{for } 9 \leqslant i \leqslant 12 \\ 2c(\pm1, \pm1) & \text{for } 13 \leqslant i \leqslant 16, \\ \text{cyc} : 3c(\pm1,0) & \text{for } 17 \leqslant i \leqslant 20 \\ 3c(\pm1, \pm1) & \text{for } 21 \leqslant i \leqslant 24 \\ c(3,1), -c(3,1) & \text{for } 25 \leqslant i \leqslant 26 \end{cases} \quad (27)$$

where "cyc" indicates the cyclic permutation. For $1 \leqslant i \leqslant 4$, $\eta_i = i\eta_0$; for $5 \leqslant i \leqslant 8$, $\eta_i = (i-4)\eta_0$; otherwise, $\eta_i = 0$. The choosing of $\mathbf{v}_{25}$ is flexible as long as $\mathbf{v}_{25} = -\mathbf{v}_{26}$, where c and η_0 are two free parameters, adjusted to guarantee the existence of $\mathbf{C}^{-1}$ and to optimize the properties of the model. The specific-heat ratio can be defined as $\gamma = c_p/c_v = (n+4)/(n+2)$.

After the accomplishment of physical modeling, we solve Eq. (1) to update f_i via finite difference schemes. Physical quantities, such as density, velocity, temperature, pressure, viscous stress, and heat flux are calculated from kinetic moments of f_i and equation of state: $\rho = \sum_i f_i$, $\mathbf{u} = \sum_i f_i\mathbf{v}_i/\rho$, $T = \frac{1}{(n+2)R}[\sum_i f_i(v_i^2+\eta_i^2)/\rho - u^2]$, $P = \rho RT$, $\mathbf{\Delta}_2^* = \sum_i (f_i - f_i^{(0)})\mathbf{v}_i^*\mathbf{v}_i^*$ and $\mathbf{\Delta}_{3,1}^* = \sum_i (f_i - f_i^{(0)})\frac{v_i^{*2}+\eta_i^2}{2}\mathbf{v}_i^*$.

It is noteworthy that: (a) The approach for calculating DEDF is general, straightforward, and independent of the Gaussian quadrature formula. (b) The number of discrete velocities used here can be as small as that of the independent kinetic moment relations. Compared with other kinetic methods, DBM adapts the minimal set of discrete velocities and consequently it enjoys a high computational efficiency. (c) The model casts off the standard "propagation + collision" mode and frees from the combination of spatial and temporal discretizations. The sets of particle velocities are highly flexible in magnitude and number, which substantially improves the numerical stability, and consequently, is much more convenient to meet the requirements for simulating compressible flows. (d) To access the behavior of the system farther away from equilibrium, one needs to add more kinetic moment relations into $\Psi(\mathbf{v}_i, \eta_i)$. Then $\Psi(\mathbf{v}_i, \eta_i)$ owns more elements and $f_i^{(0)}$ becomes more complicated, and more discrete velocities are needed. Compared with the corresponding hydrodynamic equations whose complexity will sharply increase with increasing the degree of TNE effects, the modeling process of DBM is only mildly affected. This is a major benefit of the discrete velocity representation versus the hierarchical Hermite expansion, which generates highly nonlinear tensors at each increasing order. (e) Being able to recover the NS (Burnett) model is only one of the functions of the DBM. The DBM presents a kind of new approach and a set of convenient and efficient tools to describe, measure, and analyze the nonequilibrium behaviors, by calculating the difference between kinetic moments of discrete distribution functions and DEDF, $\mathbf{\Delta}_m = \mathbf{M}_m(f - f^{(0)})$ and $\mathbf{\Delta}_m^* = \mathbf{M}_m^*(f - f^{(0)})$. From this point of view, a DBM is roughly equivalent to a hydrodynamic model supplemented by a coarse grained model of the TNE effects. (f) At last, we stress that, via the DBM, it is straightforward to perform multiscale simulations over a wide range of Knudsen number by switching the effective parameter controlling the TNE extent. This is because the multiscale modeling of DBM is under the same framework without message passing between models at different scales. These outstanding advantages make DBM a particularly appealing methodology for investigating nonequilibrium flows.

Meanwhile, we point out that owing to the utilization of a single relaxation time in the collision term, the Prandtl number becomes fixed at a specific value $\mathrm{Pr} = 1$. To overcome this limitation, one convenient way is to add an external forcing term I_i into the right-hand side of Eq. (1) to modify the BGK collision operator [93], $I_i = [ART + B(\mathbf{v}_i - \mathbf{u})^2]f_i^{(0)}$

with $A = -2B$ and $B = \frac{1}{2\rho T^2}\nabla\cdot[\frac{4+n}{2}\rho T q \nabla T]$. As a result, the heat conductivity has been changed to be $\kappa = c_p P(\tau + q)$, and the Prandtl number $\Pr = \frac{\tau}{\tau+q}$. Besides its conciseness, more importantly, this approach does not give rise to additional kinetic moments requirement.

III. NUMERICAL SIMULATIONS AND ANALYSIS

In this section, several typical benchmarks, ranging from subsonic to hypersonic, are conducted to validate the model. Afterwards, we investigate carefully the performances of the new model for describing compressible flows over a wide range of Knudsen numbers. To improve the numerical stability, efficiency, and to accurately capture the complex characteristic structures, the third-order implicit-explicit Runge-Kutta finite difference scheme [94] is adopted to discretize the temporal derivative; the second-order nonoscillatory non-free-parameter and dissipative finite difference (FD) scheme is used to discretize the spatial derivatives for the second and third Riemann problems; for other problems considered, the fifth-order weighted essentially nonoscillatory FD scheme is applied to calculate the spatial derivatives. The adoption of the FD scheme makes the boundary condition (BC) easily incorporated into the model, which is exactly the same as that implemented in the conventional computational fluid dynamics (CFD) methods. The discrete Boltzmann equation, particle velocity, and hydrodynamic quantities have been nondimensionalized by suitable reference variables [95]. Among which, three independent ones are the characteristic flow length scale L_0, the reference density ρ_0, and the reference temperature T_0. The other characteristic variables are defined as $u_0 = \sqrt{RT_0}$, $t_0 = L_0/u_0$, and $P_0 = \rho_0 R T_0$. In our simulations, we assume that the fluid is air under normal conditions, then the scales used to specify the magnitudes of the density, temperature, fluid velocity components are $\rho_0 = 1.165\,\mathrm{kg/m^3}$, $T_0 = 303\,\mathrm{K}$, and $u_0 = \sqrt{RT_0} \approx 294.892\,\mathrm{m/s}$ with $R = 287\,\mathrm{J/(kg\,K)}$, respectively.

A. Riemann problems

1. Sod shock tube

The first test case is the standard Sod shock tube problem with the following initial conditions,

$$(\rho,T,u_x,u_y)|_L = (1.0,1.0,0.0,0.0),$$
$$(\rho,T,u_x,u_y)|_R = (0.125,0.8,0.0,0.0), \tag{28}$$

where subscripts "L" and "R" stand for macroscopic variables at the left and right sides of the discontinuity. It is a classical test in the study of compressible flows that consists of (i) a shock wave propagating into the low pressure region, (ii) a rarefaction wave expanding into the high pressure part, and (iii) a contact discontinuity moving rightward. The periodic BC is imposed in the y direction. In the x direction, we apply the supersonic inflow BC [96,97], i.e., $f_{i,-2,t} = f_{i,-1,t} = f_{i,0,t} = f^{(0)}_{i,1,t=0}$, where -2, -1, and 0 are indexes of three ghost nodes out of the left boundary. Such a BC means that the system at the boundary stays as their corresponding equilibrium state, or in other words, the macroscopic quantities on the boundary

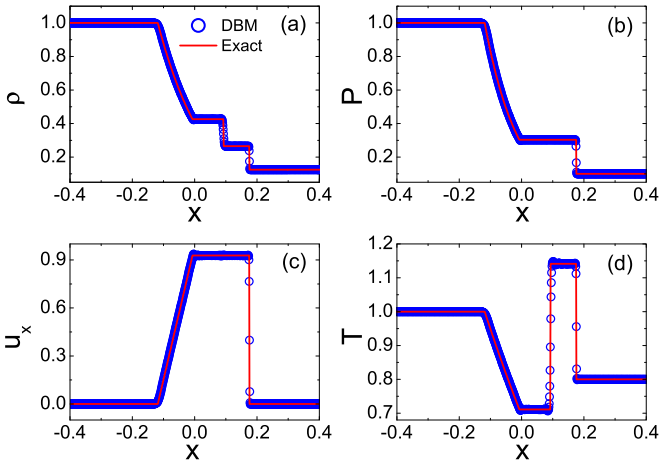

FIG. 3. Comparisons between DBM simulations and the exact solutions for the Sod shock tube, where $t = 0.1$ and $\gamma = 1.4$. (a) Density, (b) pressure, (c) velocity, and (d) temperature.

nodes keep at their initial values $(\rho,\mathbf{u},T)_{-2,t} = (\rho,\mathbf{u},T)_{-1,t} = (\rho,\mathbf{u},T)_{0,t} = (\rho,\mathbf{u},T)_{1,t=0}$. On the right side, we can operate in a similar way. BC implemented on the distribution function and macroscopic quantities may be referred to as the mesoscopic BC and the macroscopic BC, respectively, which are consistent with each other. Moreover, when the external environment is out-of-equilibrium, the nonequilibrium part $f^{(\mathrm{neq})}_{i,I}$ can be obtained from the inner lattice nodes via the extrapolation method, which is a merit of DBM over the traditional CFD. BCs for the following test cases are consistent with what we imposed above. Parameters are set to be $\Delta x = \Delta y = 10^{-3}$, $\Delta t = 10^{-4}$, $\tau = 10^{-5}$, $c = 1$, $\eta_0 = 1.5$, and $\gamma = 1.4$. The lattice points are 2000×4. Figure 3 exhibits the computed density, pressure, velocity, and temperature profiles at $t = 0.1$, where circles indicate results from DBM simulations and solid lines from Riemann solutions. The two sets of results coincide with each other. Moreover, the shock wave, expanding wave and contact discontinuity are well captured with severely curtailed numerical dissipation and effectively refrained unphysical oscillations.

2. Modified Lax shock tube

To further highlight robustness of the model, we construct a modified Lax shock tube with larger velocity difference,

$$(\rho,T,u_x,u_y)|_L = (0.445,7.928,0.698,0.0),$$
$$(\rho,T,u_x,u_y)|_R = (0.50,1.142,-0.698,0.0). \tag{29}$$

Comparisons between simulation results and the exact solutions at $t = 0.07$ are plotted in Fig. 4, where $c = 1.7$, $\eta_0 = 6.0$, and $\gamma = 2$; other parameters are unchanged. The two sets of results agree excellently with each other. Additionally, the shock wave and contact discontinuity are captured stably and no overshoots nor spurious oscillations appear. Enlargement of the shock wave parts shows that it spreads over three to four grid cells, demonstrating that the present model has a high resolving power in capturing such complex structure.

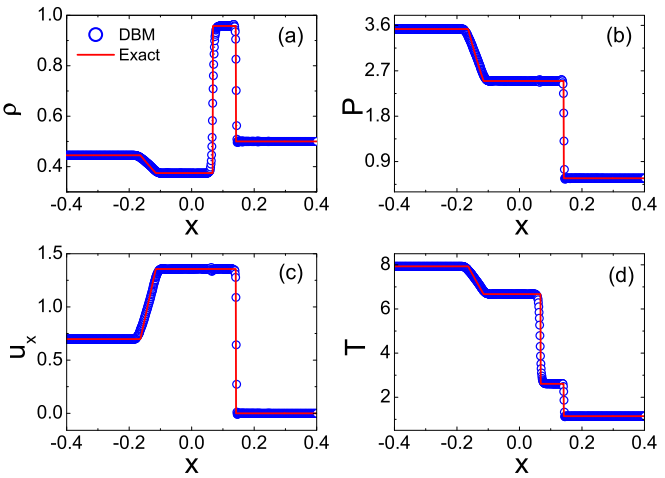

FIG. 4. Comparisons between DBM simulations and the exact solutions for the modified Lax shock tube, where $t = 0.07$ and $\gamma = 2$. (a) Density, (b) pressure, (c) velocity, and (d) temperature.

3. Collision of two strong shocks

To further examine the robustness, precision, and adaptability of the model for compressible flow with strong shock strength, we consider the collision of two strong shocks described by

$$(\rho,T,u_x,u_y)|_L = (5.99924,76.8254,19.5975,0.0),$$
$$(\rho,T,u_x,u_y)|_R = (5.99242,7.69222,-6.19633,0.0). \quad (30)$$

With respect to the former two tests, this is generally regarded as a more challenging one. Analytical solution contains a contact discontinuity moving rightward, a right-shock spreading to the right side, and a left-shock propagating rightward very slowly creating additional difficulties to the numerical scheme. Figure 5 displays comparisons between DBM results and the corresponding exact solutions, where $t = 0.05$, $\gamma = 1.67$. Parameters used here are $\Delta x = \Delta y = 4\times10^{-3}$, $\Delta t = 10^{-4}$, $\tau = 5\times10^{-5}$, $c = 9$, and $\eta_0 = 30$. One can see that our results are in satisfying agreement with the theoretical solutions with

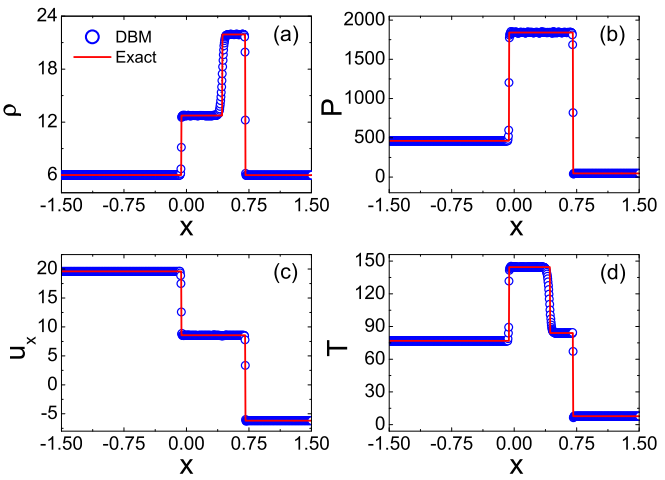

FIG. 5. Comparisons between DBM simulations and the exact solutions for the collision of two strong shocks, where $t = 0.05$ and $\gamma = 1.67$. (a) Density, (b) pressure, (c) velocity, and (d) temperature.

very correct propagation of the shocks. Successful simulation of this aggressive test manifests that the proposed model is robust, accurate, and applicable to compressible flows with strong shock wave interaction.

B. Performance of the DBM for describing higher-order TNE effects

To evaluate whether the model can describe TNE effects at various levels and whether the model can reproduce accurate viscous stress and heat flux for compressible flows over a wide range of Knudsen numbers and Mach numbers, a series of simulations for head-on collision between two shocks have been conducted. The initial configurations are

$$\rho(x,y) = \frac{\rho_L+\rho_R}{2} - \frac{\rho_L-\rho_R}{2}\tanh\left(\frac{x-N_x\Delta x/2}{L_\rho}\right), \quad (31)$$

$$u_x(x,y) = -u_0\tanh\left(\frac{x-N_x\Delta x/2}{L_u}\right), \quad (32)$$

where L_ρ and L_u are the widths of density and velocity transition layers, respectively. ρ_L (ρ_R) is the density away from the interface of the left (right) fluid. The whole computational domain is a rectangle with length 1.5 and height 0.006, divided into 1000×4 uniform meshes.

1. Viscous stress

According to the analytical expressions of TNE manifestations, two factors control their strengths and structures, the relaxation time τ and the gradient force induced by gradients of macroscopic quantities. In the first three sets of simulations, we fix variables as $\rho_L = 2\rho_R = 2$, $P_L = P_R = 2$, $u_y = 0$, $L_\rho = L_u = 20$, then adjust τ and u_0, resulting in three types of viscous stresses. Figure 6 depicts the details at $t = 0.025$, where two DBMs are used: the D2V16 model at the NS level [left column, satisfies the former 7 kinetic moments, Eqs. (2)–(6) and Eqs. (18) and (19)], and the D2V26 model at the Burnett level [right column, satisfies all needed kinetic moments, Eqs. (2)–(6) and Eqs. (18)–(21)]. For comparisons, the analytical solutions with the first and second order accuracies calculated from Eqs. (22), (23), (A1), and (A4) are plotted in each panel by dashed and solid lines, respectively.

Figure 6 qualitatively reveals the common features during the procedure deviating from thermodynamic equilibrium: (i) TNE effects are mainly around the contact interface where the gradients of macroscopic quantities are pronounced and exactly attain their local maxima (minima) at the points of the maxima $(\nabla\rho,\nabla T,\nabla u_x)_{\max}$, for example, at $x = 477$ and 522, while they tend to vanish where the TNE driving force is nearly zero. Behaviors of TNE can be well interpreted by our theoretical formulations. (ii) For all cases, the first-order NOMF $\Delta^{*(1)}_{2xx}$, linearly proportional to τ, is larger than the second-order NOMF $\Delta^{*(2)}_{2xx}$, proportional to τ^2, numerically manifesting that $\Delta^{*(1)}_{2xx}$ is the leading part of Δ^{*}_{2xx} and the appropriateness of NS model as a coarse-grained model for compressible flows.

Apart from similarities, the following distinctive differences between various cases and models deserve more attention. Different relaxation times and shock intensities generate different

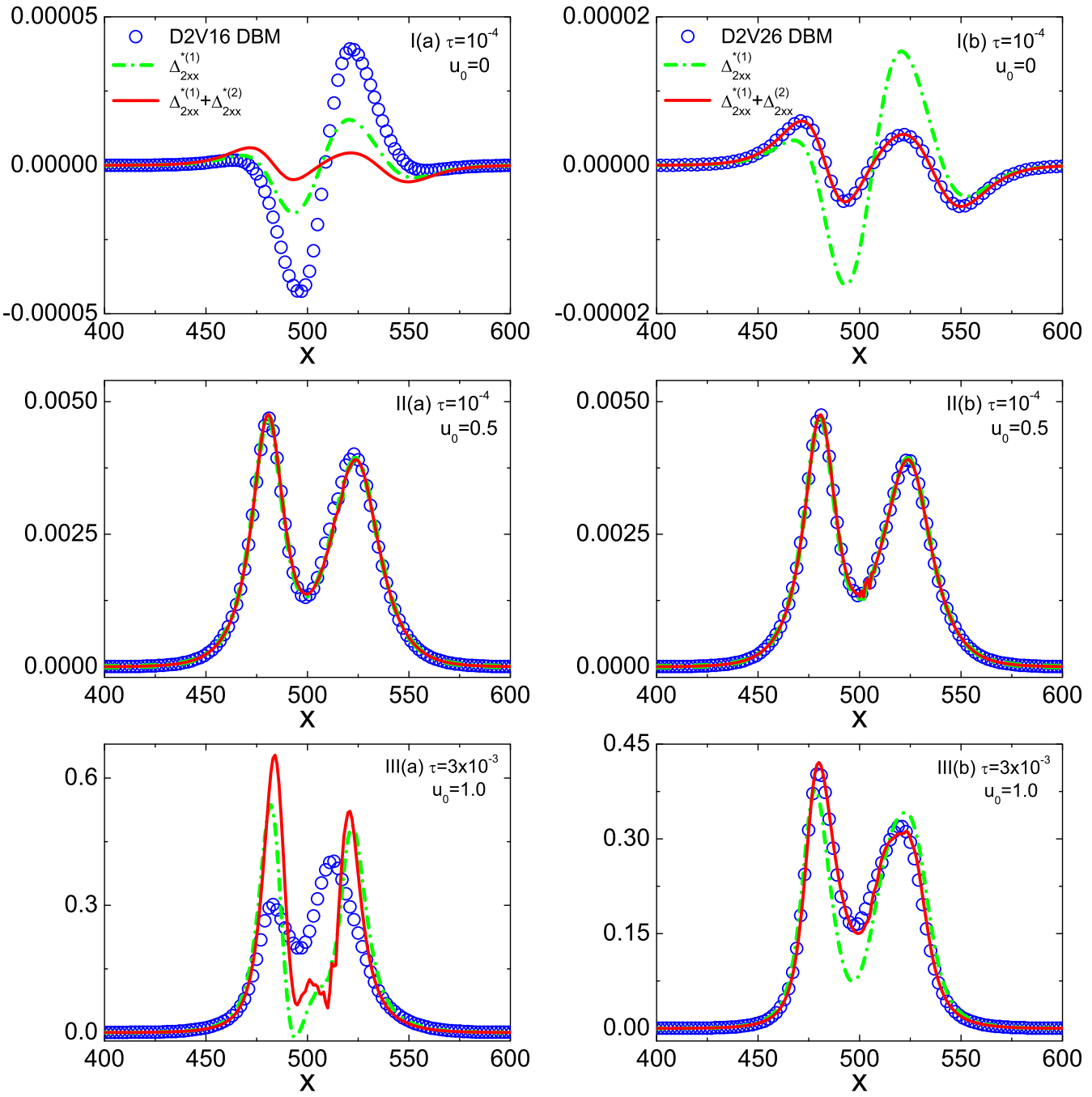

FIG. 6. Viscous stress calculated from D2V16 (left column) and D2V26 (right column) DB simulations (scatters) for the weak (I), moderate (II), and strong (III) cases, where dashed and solid lines indicate analytical solutions with first- and second-order accuracies, respectively.

TNE amplitudes. For case I (first row), due to lack of velocity gradient ($\mathbf{u} = 0$), at the beginning, viscous stress is only induced by gradients of density and temperature. Therefore, $\Delta_{2xx}^{*(2)} > \Delta_{2xx}^{*(1)} \simeq 0$. Afterwards, the density and temperature gradients stimulate velocity gradients, then $\Delta_{2xx}^{*(1)}$ becomes gradually larger than $\Delta_{2xx}^{*(2)}$. In both cases, smaller τ and the initially static fluid lead to weaker TNE effects. Nevertheless, even for such a very tiny TNE amplitude, remarkable discrepancies appear between the D2V16 simulations and the theoretical predictions, regardless of the first-order or the second-order one [see Fig. 6, panel I(a)]. On the contrary, the D2V26 result agrees well with the theoretical solution at the second-order $\Delta_{2xx}^{*(1)} + \Delta_{2xx}^{*(2)}$ [see Fig. 6, panel I(b)]. The D2V16 model is accurate at the NS level, without considering the second-order TNE effects, and therefore it is not suitable for simulating cases when $\Delta_{2xx}^{*(2)}$ is as important as $\Delta_{2xx}^{*(1)}$. For case II (second row), we increase the intensity of TNE through increasing the collision velocity. As a result, Δ_{2xx}^{*} is 100 times larger than that in case I, and $\Delta_{2xx}^{*(2)}$ is negligible compared with $\Delta_{2xx}^{*(1)}$, demonstrating that the velocity gradient acts as the dominating factor for TNE intensity. Excellent agreements between DBM simulations and theoretical solutions are found

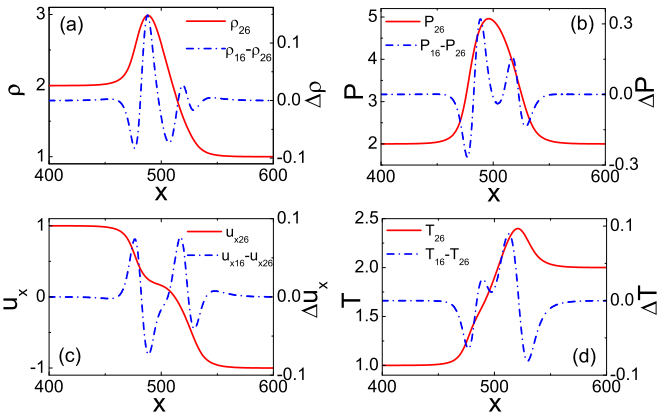

FIG. 7. Hydrodynamic quantities calculated from the D2V26 model and the corresponding differences between the D2V26 and D2V16 models at $t = 0.025$ for case III. (a) Density, (b) pressure, (c) velocity, and (d) temperature.

for both models [see Fig. 6, panels II(a) and II(b)]. Further increase in relaxation time and collision velocity give rise to more prominent TNE phenomena and more remarkable deviation from the Maxwellian distribution, as shown in case III (third row). We observe that, larger velocity not only induces a huge first-order TNE $\Delta_{2xx}^{*(1)}$, but also prominently triggers the gradients in density and temperature (see Fig. 7 for more details), and consequently, results in considerable second-order TNE $\Delta_{2xx}^{*(2)}$. The D2V16 model fails to tame such strong TNE behaviors, while the D2V26 model succeeds [see Fig. 6, panels III(a) and III(b)].

Usually, the local Knudsen number, defined as the ratio of molecular mean-free-path to a local characteristic length scale $\mathrm{Kn} = \lambda/L$, is one of the main parameters employed to describe the level of nonequilibrium, where $\lambda = c_s\tau$, c_s is the local speed of sound, L can be defined in terms of the macroscopic gradients, e.g., $L = \phi/|\nabla\phi|$. The maxima $\mathrm{Kn}_{\max}$ for cases I, II, and III are 0.0018, 0.003, and 0.15, respectively, all beyond the application scope of the NS model. Actually, the D2V26 model has been extended into the early transition regime. It is also interesting to note that the D2V16 model is more reliable and more powerful to study case II than case I. Thus, from this point of view, the Knudsen number is not sufficient enough to describe the TNE extent for cases with small Mach numbers. To complement this deficiency, we introduce another dimensionless parameter to characterize the relative TNE intensity, $R_{\mathrm{TNE}} = |\Delta_2^{*(2)}/\Delta_2^{*(1)}|$. For the three cases, $R_{\mathrm{TNE}} = 0.69$, 0.01, 0.42, respectively. Consequently, higher-order DBMs are needed for cases I and III, even though the TNE intensity is weak in case I. It is convenient to generalize the definition as $R_{\mathrm{TNE}} = |\Delta_{m,n}^{*(N+1)}/\Delta_{m,n}^{*(N)}|$, where $\Delta_{m,n}^{*(N+1)}$ ($\Delta_{m,n}^{*(N)}$) is the $(N+1)$th (Nth) order TNE. Meanwhile, we can define the TNE discrepancy between DBM simulation and the corresponding theoretical analysis, $\varrho = \Delta_{\mathrm{DBM}} - \Delta_{\mathrm{Exact}}$. These two measures provide as effective physical criteria to assess whether the current DBM is appropriate or not. In real simulations, only when the R_{TNE} and/or ϱ is small enough, the current DBM is suitable for describing the current problem; otherwise, higher-order TNE effects should be taken into account in the modeling and higher-order DBM should be constructed.

We also stress that the exact calculation of viscous stress and heat flux are of great importance for simulating high-speed, nonequilibrium compressible flows, because the transport and dissipation of kinetic energy and momentum resulting in complex mesoscopic structures (such as shock wave interface, material interface, Mach stem, etc.) depend strongly on them. More importantly, accurate viscous stress and heat flux are required to obtain accurate hydrodynamic quantities, as demonstrated by Fig. 7, where $\phi_{16} - \phi_{26}$ indicates hydrodynamic quantities differences between the D2V16 and D2V26 models for case III. It is clear that the differences, up to 10% of the exact solutions, are around the highly nonequilibrium regimes. The inaccuracies of the D2V16 model are due to the lack of some necessary kinetic moments required for recovering $f^{(2)}$.

To further examine the reliability of D2V26 model in describing much stronger TNE effects, we increase τ to 6×10^{-3} and $u_0 = 1.7$. Shown in Fig. 8 are viscous stress [Fig. 8(a)] for the very accentuated case and the local Knudsen numbers

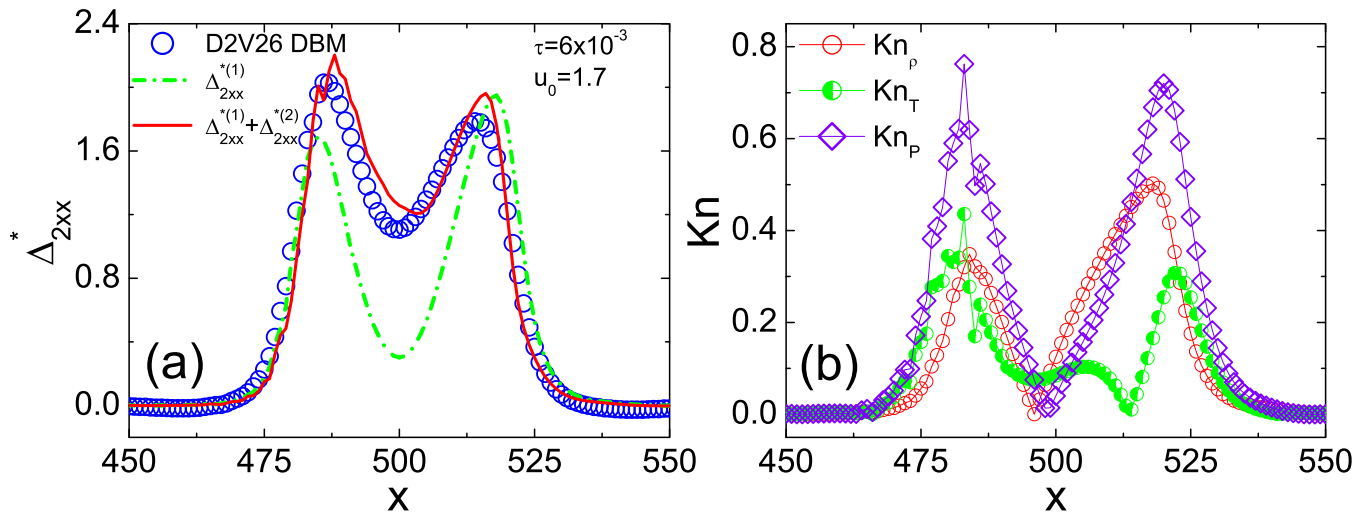

FIG. 8. Viscous stress for the very strong case (a) and the local Knudsen numbers calculated from pressure, density, and temperature (b).

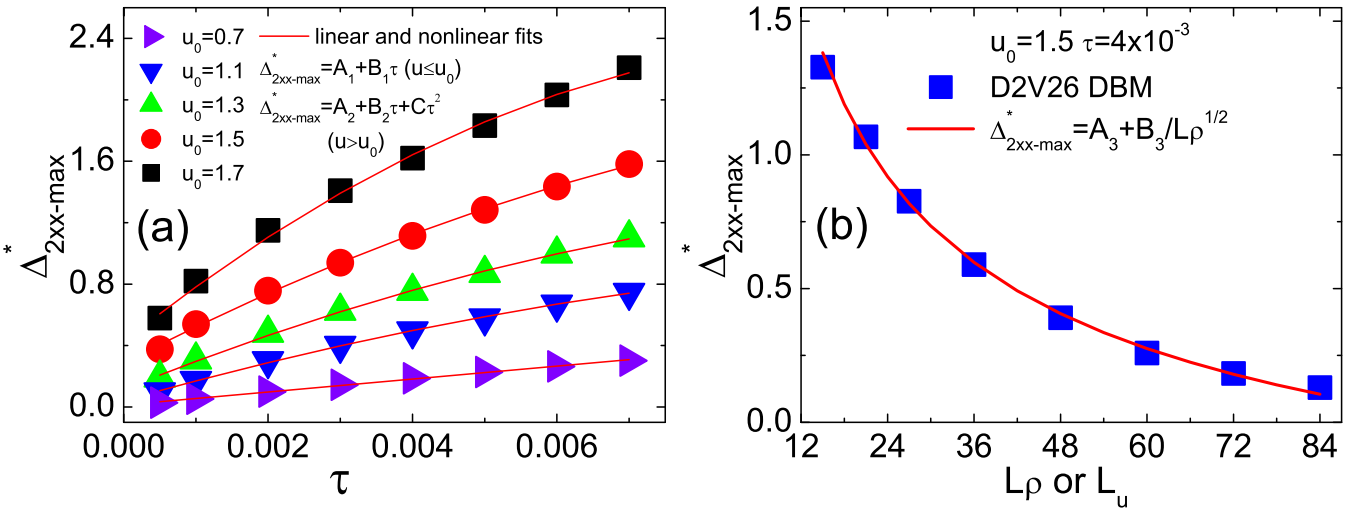

FIG. 9. Effects of shock intensity (a) and interface width (b) on TNE effects.

[Fig. 8(b)] calculated from pressure, density, and temperature, respectively. Good agreement between the DBM simulation and the second-order theoretical solution can be found. The maximum Knudsen number calculated from density exceeds 0.5, and the one calculated from pressure is as high as 0.8. When the strength of TNE further increases, the presented model loses its effectiveness and effects of $f^{(3)}$ should be taken into account.

Effects of shock intensity and interface width on TNE manifestations are investigated similarly. As plotted in Fig. 9(a), the maximum nonequilibrium stress increases with both τ and u_0. The relationship between $\Delta^*_{2xx-\max}$ and τ can be further divided into two cases: linear and nonlinear. When u_0 is less than a critical value u_c, say 0.7, $\Delta^*_{2xx-\max}$ increases linearly with τ, $\Delta^*_{2xx-\max} = A_1 + B_1\tau$; when $u_0 > u_c$, a nonlinear fitting is more approximate, $\Delta^*_{2xx-\max} = A_2 + B_2\tau + C_2\tau^2$, demonstrating the necessity of a higher-order constitutive relations for cases far-away-from-equilibrium. Conversely, the interface width effects decrease the maximum of Δ^*_{2xx} approximately in the following way, $\Delta^*_{2xx-\max} = A_3 + \frac{B_3}{L^{1/2}}$, with $A_3 = -0.81$ and $B_3 = 8.47$, as shown in Fig. 9(b). This conclusion is consistent with the effects of surface tension that controls the width of hydrodynamic quantities in multiphase flows [61]. Physically, the interface width lowers the gradient force and suppresses the TNE intensity.

2. *Heat flux*

The viability of the D2V26 model for describing higher-order heat flux is verified in a similar way. Consistently, three cases are considered, with the following initial variables, case I: $T_L = T_R = 1$, $P_L = 1$, P_R=2, $\tau = 10^{-3}$; case II: $T_L = 2T_R = 1.2$, $P_L = P_R = 1.2$, $\tau = 5\times10^{-4}$; case III: $T_L = 2T_R = 1.2$, $P_L = P_R = 1.2$, $\tau = 2\times10^{-3}$. Collision velocity for all cases is fixed to be $u_0 = 0.5$. Figure 10 presents the details, where $t = 10^{-3}$ in case II and $t = 9\times10^{-3}$ in the other two cases. For the first case, temperature is initially homogeneous, thus $\Delta^{*(1)}_{3,1x}$ approaches nearly zero at the beginning stage. The second-order heat flux $\Delta^{*(2)}_{3,1x}$ is motivated exclusively by a pressure difference. After that, gradients appear in each quantity resulting in the emergence of the first-order heat flux. At the moment shown in case I, the relative intensity $R_{\rm TNE} = \Delta^{*(2)}_{3,1x}/\Delta^{*(1)}_{3,1x}$ is about 0.98. As excepted, the D2V16 model fails to predict this situation although with weak TNE intensity [see Fig. 10, panel I(a)]. Through enlarging gradient in temperature in case II, $\Delta^*_{3,1x}$ is overwhelmed by $\Delta^{*(1)}_{3,1x}$, as reported in the second row of Fig. 6. For this case, the two models recover favorable results [see panels Fig. 10, panels II(a) and II(b)]. The deficiency of the D2V16 model and the sufficiency of the D2V26 model for portraying TNE with higher amplitude, has been witnessed by case III [see Fig. 10, panels III(a) and III(b)], again.

IV. CONCLUSIONS AND REMARKS

A framework for constructing the trans-scale DBM that aims to investigate high-speed compressible flows ranging from continuum to transition regime is presented. In this framework, the specific forms of the extremely complex Burnett, even super-Burnett, equations are not needed. To access higher-order nonequilibrium effects, the extension of the framework and the construction of corresponding DBM are more convenient and straightforward than the extended hydrodynamic equations; the complexity of the DBM increases only mildly, as opposed to the sharp rise of complexity of the thermohydrodynamic equations. Through switching the effective parameter that controls the TNE extent, one can perform multiscale simulations over a wide range of Knudsen number under the same framework without message passing between models at different scales. As a model example, a two-dimensional DBM with 26 discrete velocities at Burnett level is formulated, verified, and validated. As by-products, the linear and nonlinear constitutive relations for the hydrodynamic modeling are derived, which contribute to improve the macroscopic modeling. To better characterize the nonequilibrium flows and understand the conditions under which the DBMs at various levels must be used, besides some higher-order kinetic moments of $(f - f^{(0)})$ and the Knudsen number,

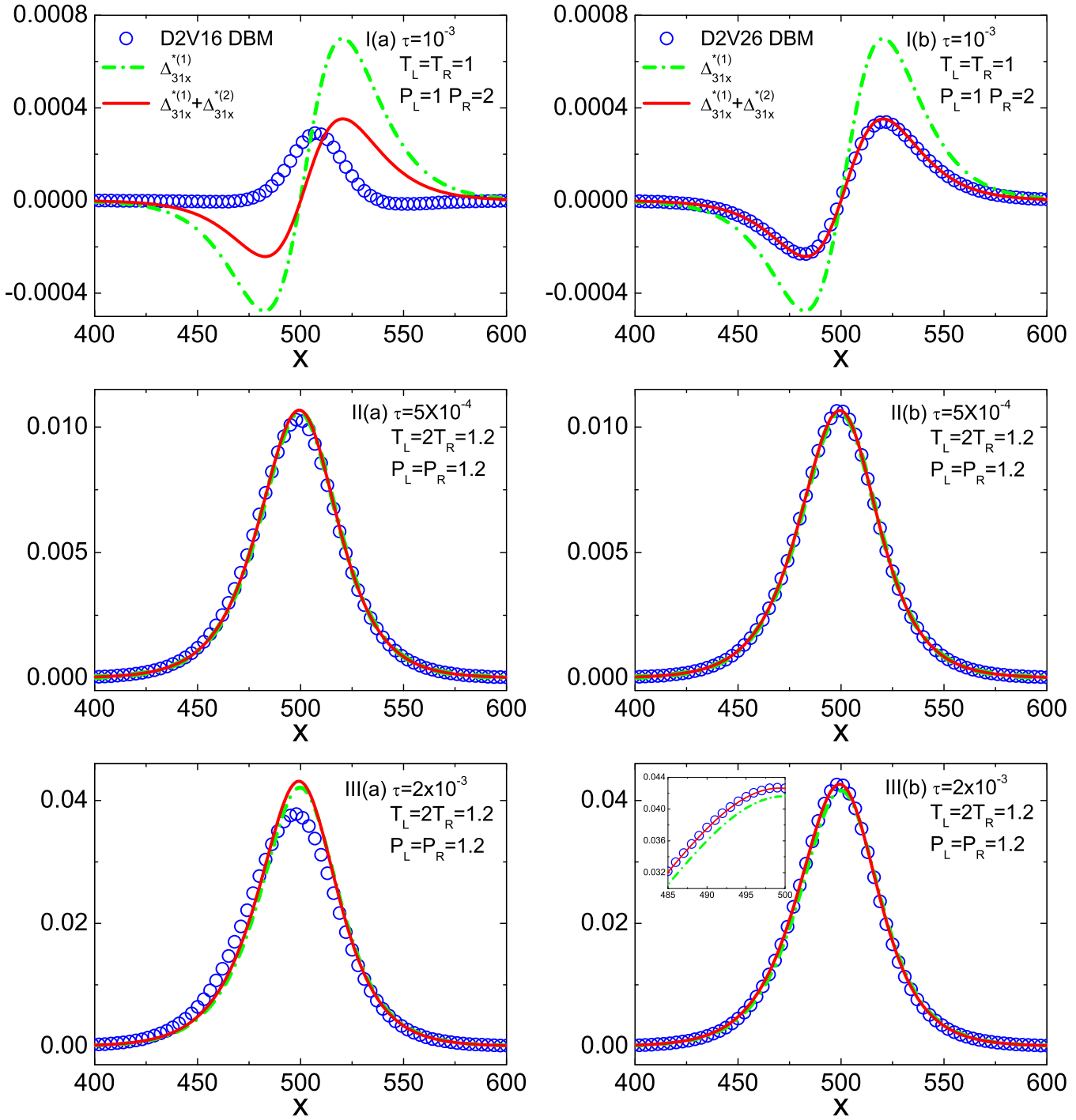

FIG. 10. Heat flux calculated from D2V16 (left column) and D2V26 (right column) DBM simulation (scatters) for the weak (I), moderate (II), and strong (III) cases, where dashed and solid lines indicate analytical solutions with first- and second-order accuracies, respectively.

two additional criteria, i.e., (i) the relative TNE strength, describing the relative strength of the $(N+1)$th order TNE to the Nth order one, and (ii) the TNE discrepancy between DBM simulation and corresponding theoretical analysis, are defined. Whether or not the higher-order TNE effects should be taken into account in the modeling process and which level of DBM should be utilized depends on the relative strength of the higher-order TNE with respect to the current order and/or the TNE discrepancy, instead of the value of Knudsen number itself.

ACKNOWLEDGMENTS

The authors sincerely thank the anonymous reviewers for their valuable comments and suggestions, which were very helpful for revising the manuscript. Also, we warmly thank Prof. Yonghao Zhang, Prof. Zhihui Li, Dr. Lei Wu, Dr. Jianping Meng, Dr. Chuandong Lin, Dr. Ge Zhang, Dr. Huilin Lai, and Dr. Bohai Chen for many instructive discussions. We acknowledge support from the National Natural Science Foundation of China (Grants No. 11475028, No. 11772064,

and No. 11602162), Science Challenge Project (Grant No. JCKY2016212A501), Natural Science Foundation of Hebei Province (Grants No. A2017409014 and No. A201500111), Natural Science Foundations of Hebei Educational Commission (Grant No. ZD2017001) and FJKLMAA, Fujian Normal University (Grant No. FJKLMAA1710).

APPENDIX: FORMULATIONS OF THE SECOND-ORDER VISCOUS STRESS AND HEAT FLUX

$$\begin{aligned}\Delta^{*(2)}_{2xx} = {} & 2n_2^{-2}\tau^2\Big\{\rho RT[n_{-2}n_1(\partial_x u_x)^2 + n_1 n_2(\partial_y u_x)^2 \\ & - 4n\,\partial_x u_x \partial_y u_y - n_2(\partial_x u_y)^2 \\ & - n_{-2}\,(\partial_y u_y)^2] + \rho R^2[n_1 n_2(\partial_x T)^2 - n_2(\partial_y T)^2] \\ & - R^2T^2\left[n_1 n_2 \frac{\partial^2}{\partial x^2}\rho - n_2\frac{\partial^2}{\partial y^2}\rho\right] \\ & + \frac{R^2T^2}{\rho}[n_1 n_2(\partial_x\rho)^2 - n_2(\partial_y\rho)^2]\Big\}, \end{aligned} \tag{A1}$$

$$\begin{aligned}\Delta^{*(2)}_{2xy} = {} & 2\tau^2\Big[n_2^{-1}\rho T(n\partial_x u_x\partial_x u_y + n\partial_y u_x\partial_y u_y \\ & - 2\partial_x u_y\partial_y u_y - 2\partial_x u_x\partial_y u_x) + \rho R^2\partial_x T\partial_y T \\ & - R^2T^2\frac{\partial^2}{\partial x\partial y}\rho + \frac{R^2T^2}{\rho}\partial_x\rho\partial_y\rho\Big], \end{aligned} \tag{A2}$$

$$\begin{aligned}\Delta^{*(2)}_{2yy} = {} & -2n_2^{-2}\tau^2\Big\{\rho RT[n_{-2}(\partial_x u_x)^2 + n_2(\partial_y u_x)^2 \\ & + 4n\,\partial_x u_x\partial_y u_y - n_1 n_2(\partial_x u_y)^2 \\ & - n_{-2}n_1\,(\partial_y u_y)^2] + \rho R^2[n_2(\partial_x T)^2 - n_1 n_2(\partial_y T)^2] \\ & - R^2T^2\left[n_2\frac{\partial^2}{\partial x^2}\rho - n_1 n_2\frac{\partial^2}{\partial y^2}\rho\right] \\ & + \frac{R^2T^2}{\rho}[n_2(\partial_x\rho)^2 - n_1 n_2(\partial_y\rho)^2]\Big\}, \end{aligned} \tag{A3}$$

$$\begin{aligned}\Delta^{*(2)}_{3,1x} = {} & n_2^{-1}\tau^2\Big\{\rho R^2T^2\left[n_{-2}\frac{\partial^2}{\partial x^2}u_x + n_2\frac{\partial^2}{\partial y^2}u_x - 4\frac{\partial^2}{\partial x\partial y}u_y\right] \\ & + \rho R^2T\left[\left(n_2^2+4n\right)\partial_x u_x\partial_x T + n_2 n_6\partial_y u_x\partial_y T\right. \\ & \left. - 2n_6\partial_y u_y\partial_x T + 2n_2\partial_x u_y\partial_y T\right]\Big\}, \end{aligned} \tag{A4}$$

$$\begin{aligned}\Delta^{*(2)}_{3,1y} = {} & n_2^{-1}\tau^2\Big\{\rho R^2T^2\left[n_2\frac{\partial^2}{\partial x^2}u_y + n_{-2}\frac{\partial^2}{\partial y^2}u_y - 4\frac{\partial^2}{\partial x\partial y}u_x\right] \\ & + \rho R^2T\left[\left(n_2^2+4n\right)\partial_y u_y\partial_y T + n_2 n_6\partial_x u_y\partial_x T\right. \\ & \left. - 2n_6\partial_x u_x\partial_y T + 2n_2\partial_y u_x\partial_x T\right]\Big\}, \end{aligned} \tag{A5}$$

where $n_a = n + a$.

[1] A. Xu, G. Zhang, Y. Ying, and C. Wang, Sci. China: Phys., Mech. Astron. **59**, 650501 (2016).
[2] Y. Ju and K. Maruta, Prog. Energy Combust. Sci. **37**, 669 (2011).
[3] G. R, Nigri, S. Tsai, S. Kossodo, P. Waterman, P. Fungaloi, D. C. Hooper, A. G. Doukas, and G. M. Lamuraglia, Lasers Surg. Med. **29**, 448 (2001).
[4] J. J. Rassweiler, T. Knoll, K. U. Köhrmann, J. A. Mcateer, J. E. Lingeman, R. O. Cleveland, M. R. Bailey, and C. Chaussy, Eur. Urol. **59**, 784 (2011).
[5] N. Boussetta, E. Vorobiev, T. Reess, A. De Ferron, L. Pecastaing, R. Ruscassié, and J.-L. Lanoisellé, Innov. Food Sci. Emerg. **16**, 129 (2012).
[6] Z. H. Li and H. X. Zhang, J. Comput. Phys. **193**, 708 (2004).
[7] Z. H. Li and H. X. Zhang, J. Comput. Phys. **228**, 1116 (2009).
[8] Z. H. Li, A. P. Peng, H. X. Zhang, and J. Y. Yang, Prog. Aerosp. Sci. **74**, 81 (2015).
[9] Z. H. Wang, *Theoretical Modelling of Aeroheating on Sharpened Noses Under Rarefied Gas Effects and Nonequilibrium Real Gas Effects* (Springer, New York, 2014).
[10] H. Liu, W. Kang, H. Duan, P. Zhang, and X. He, Sci. China: Phys., Mech. Astron. **47**, 070003 (2017).
[11] L. Wang, W. Ye, X. He, J. Wu, Z. Fan, C. Xue, H. Guo, W. Miao, Y. Yuan, J. Dong, G. Jia, J. Zhang, Y. Li, J. Liu, M. Wang, Y. Ding, and W. Zhang, Sci. China: Phys., Mech. Astron. **60**, 055201 (2017).
[12] R. Balakrishnan, J. Fluid Mech. **503**, 201 (2004).
[13] H. Chen, S. Kandasamy, S. Orszag, R. Shock, S. Succi, and V. Yakhot, Science **301**, 633 (2003).
[14] W. J. Morokoff and R. E. Caflisch, J. Comput. Phys. **122**, 218 (1995).
[15] R. E. Caflisch, Acta Numer. **7**, 1 (1998).
[16] L. Pareschi and R. E. Caflisch, J. Comput. Phys. **154**, 90 (1999).
[17] S. Succi, *The Lattice Boltzmann Equation for Fluid Dynamics and Beyond* (Oxford University Press, New York, 2001).
[18] S. Succi, Europhys. Lett. **109**, 50001 (2015).
[19] H. Struchtrup, *Macroscopic Transport Equations for Rarefied Gas Flows* (Springer, New York, 2005).
[20] K. Xu, *Direct Modeling for Computational Fluid Dynamics: Construction and Application of Unified Gas-kinetics Schemes* (World Scientific Publishing, Beijing, 2015).
[21] Z. Guo and C. Shu, *Lattice Boltzmann Method and its Applications in Engineering* (World Scientific Publishing, Beijing, 2013).
[22] L. Wu, J. M. Reese, and Y. Zhang, J. Fluid Mech. **746**, 53 (2014).
[23] L. Wu, J. Zhang, J. M. Reese, and Y. Zhang, J. Comput. Phys. **298**, 602 (2015).
[24] L. M. Yang, C. Shu, J. Wu, and Y. Wang, J. Comput. Phys. **306**, 291 (2016).
[25] L. M. Yang, C. Shu, J. Wu, N. Zhao, and Z. L. Lu, J. Comput. Phys. **255**, 540 (2013).
[26] L. M. Yang, C. Shu, and J. Wu, J. Comput. Phys. **274**, 611 (2014).
[27] L. M. Yang, C. Shu, and Y. Wang, Phys. Rev. E **93**, 033311 (2016).

[28] L. M. Yang, C. Shu, Y. Wang, and Y. Sun, J. Comput. Phys. **319**, 129 (2016).
[29] Z. Guo, R. Wang, and K. Xu, Phys. Rev. E **91**, 033313 (2015).
[30] P. Wang, L.-P. Wang, and Z. Guo, Phys. Rev. E **94**, 043304 (2016).
[31] C. Liu, K. Xu, Q. Sun, and Q. Cai, J. Comput. Phys. **314**, 305 (2016).
[32] T. Xiao, Q. Cai, and K. Xu, J. Comput. Phys. **332**, 475 (2017).
[33] H. Struchtrup and M. Torrilhon, Phys. Fluids **15**, 2668 (2003).
[34] M. Torrilhon and H. Struchtrup, J. Fluid Mech. **513**, 171 (2004).
[35] H. Struchtrup and M. Torrilhon, Phys. Rev. Lett. **99**, 014502 (2007).
[36] M. Yu. Timokhin, H. Struchtrup, A. A. Kokhanchik, and Ye. A. Bondar, Phys. Fluids **29**, 037105 (2017).
[37] X. Gu and D. R. Emerson, J. Fluid Mech. **636**, 177 (2009).
[38] R. O. Fox, J. Comput. Phys. **227**, 6313 (2008).
[39] R. O. Fox, J. Comput. Phys. **228**, 7771 (2009).
[40] M. Icardi, P. Asinari, D. L. Marchisio, S. Izquierdo, and R. O. Fox, J. Comput. Phys. **231**, 7431 (2012).
[41] R. Benzia, S. Succi, and M. Vergassolac, Phys. Rep. **222**, 145 (1992).
[42] S. Succi, O. Filippova, G. Smith, and E. Kaxiras, Comput. Sci. Eng. **3**, 26 (2001).
[43] S. Succi, I. V. Karlin, and H. Chen, Rev. Mod. Phys. **74**, 1203 (2002).
[44] A. Xu, G. Zhang, Y. Gan, F. Chen, and X. Yu, Front. Phys. **7**, 582 (2012).
[45] A. J. Wagner and J. M. Yeomans, Phys. Rev. Lett. **80**, 1429 (1998).
[46] A. J. Wagner and J. M. Yeomans, Phys. Rev. E **59**, 4366 (1999).
[47] D. Marenduzzo, E. Orlandini, M. E. Cates, and J. M. Yeomans, Phys. Rev. E **76**, 031921 (2007).
[48] A. Doostmohammadi, S. P. Thampi, and J. M. Yeomans, Phys. Rev. Lett. **117**, 048102 (2016).
[49] A. J. Wagner and K. Strand, Phys. Rev. E **94**, 033302 (2016).
[50] S. Ansumali and I. V. Karlin, Phys. Rev. Lett. **95**, 260605 (2005).
[51] M. Atif, P. K. Kolluru, C. Thantanapally, and S. Ansumali, Phys. Rev. Lett. **119**, 240602 (2017).
[52] H. Huang and X.-Y. Lu, J. Fluid Mech. **822**, 664 (2017).
[53] Y. Gan, A. Xu, G. Zhang, and Y. Yang, Europhys. Lett. **103**, 24003 (2013).
[54] C. Lin, A. Xu, G. Zhang, Y. Li, and S. Succi, Phys. Rev. E **89**, 013307 (2014).
[55] A. Xu, C. Lin, G. Zhang, and Y. Li, Phys. Rev. E **91**, 043306 (2015).
[56] L. M. Yang, C. Shu, and J. Wu, Comput. Fluids **79**, 190 (2013).
[57] L. M. Yang, C. Shuc, and J. Wu, Comput. Math. Appl. **71**, 2069 (2016).
[58] Q. Li, K. H. Luo, Q. J. Kang, Y. L. He, Q. Chen, and Q. Liu, Prog. Energy Combust. Sci. **52**, 62 (2016).
[59] B. I. Green and P. Vedula, J. Stat. Mech. (2013) P07016.
[60] M. La Rocca, A. Montessori, P. Prestininzi, and S. Succi, J. Comput. Phys. **284**, 117 (2015).
[61] Y. Gan, A. Xu, G. Zhang, and S. Succi, Soft Matter **11**, 5336 (2015).
[62] H. Lai, A. Xu, G. Zhang, Y. Gan, Y. Ying, and S. Succi, Phys. Rev. E **94**, 023106 (2016).
[63] C. Lin, A. Xu, G. Zhang, and Y. Li, Combust. Flame **164**, 137 (2016).
[64] Y. Zhang, A. Xu, G. Zhang, C. Zhu, and C. Lin, Combust. Flame **173**, 483 (2016).
[65] C. Lin, A. Xu, G. Zhang, K. H. Luo, and Y. Li, Phys. Rev. E **96**, 053305 (2017).
[66] C. Lin, K. H. Luo, L. Fei, and S. Succi, Sci. Rep. **7**, 14580 (2017).
[67] C. Lin and K. H. Luo, Comput. Fluids **166**, 176 (2018).
[68] S. Ansumali, I. V. Karlin, S. Arcidiacono, A. Abbas, and N. I. Prasianakis, Phys. Rev. Lett. **98**, 124502 (2007).
[69] W. P. Yudistiawan, S. Ansumali, and I. V. Karlin, Phys. Rev. E **78**, 016705 (2008).
[70] B. Dorschner, S. S. Chikatamarla, and I. V. Karlin, J. Fluid Mech. **824**, 388 (2017).
[71] F. Toschi and S. Succi, Europhys. Lett. **69**, 549 (2005).
[72] M. Sbragaglia and S. Succi, Phys. Fluids **17**, 093602 (2005).
[73] M. Sbragaglia and S. Succi, Europhys. Lett. **73**, 370 (2006).
[74] A. Montessori, P. Prestininzi, M. La Rocca, and S. Succi, Phys. Rev. E **92**, 043308 (2015).
[75] G. Di Staso, H. J. H. Clercx, S. Succi, and F. Toschi, J. Comput. Sci. **17**, 357 (2016).
[76] G. Di Staso, H. J. H. Clercx, S. Succi, and F. Toschi, Philos. Trans. R. Soc. London A **374**, 20160226 (2016).
[77] X. Shan, X. F. Yuan, and H. Chen, J. Fluid Mech. **550**, 413 (2006).
[78] J. Meng, Y. Zhang, and X. Shan, Phys. Rev. E **83**, 046701 (2011).
[79] J. Meng, Y. Zhang, N. G. Hadjiconstantinou, G. A. Radtke, and X. Shan, J. Fluid Mech. **718**, 347 (2013).
[80] V. Sofonea and R. F. Sekerka, Phys. Rev. E **71**, 066709 (2005).
[81] V. Sofonea and R. F. Sekerka, J. Comput. Phys. **207**, 639 (2005).
[82] M. Watari, Phys. Rev. E **79**, 066706 (2009).
[83] J. Meng and Y. Zhang, J. Comput. Phys. **258**, 601 (2014).
[84] Y. H. Zhang, X. J. Gu, R. W. Barber, and D. R. Emerson, Phys. Rev. E **74**, 046704 (2006).
[85] G. H. Tang, Y. H. Zhang, and D. R. Emerson, Phys. Rev. E **77**, 046701 (2008).
[86] H. Liu, W. Kang, Q. Zhang, Y. Zhang, H. Duan, and X. T. He, Front. Phys. **11**, 115206 (2016).
[87] H. Liu, Y. Zhang, W. Kang, P. Zhang, H. Duan, and X. T. He, Phys. Rev. E **95**, 023201 (2017).
[88] P. L. Bhatnagar, E. P. Gross, and M. Krook, Phys. Rev. **94**, 511 (1954).
[89] L. H. Holway, Phys. Fluids **9**, 1658 (1966).
[90] E. M. Shakhov, Fluid Dynam. **3**, 95 (1972).
[91] V. A. Rykov, Fluid Dynam. **10**, 959 (1976).
[92] G. Liu, Phys. Fluids A **2**, 277 (1990).
[93] Y. Gan, A. Xu, G. Zhang, and Y. Li, Commun. Theor. Phys. **56**, 490 (2011).
[94] U. M. Ascher, S. J. Ruuth, and R. J. Spiteri, Appl. Numer. Math. **25**, 151 (1997).
[95] Y. Gan, A. Xu, G. Zhang, and Y. Li, Phys. Rev. E **83**, 056704 (2011).
[96] K. Qu, C. Shu, and Y. T. Chew, Phys. Rev. E **75**, 036706 (2007).
[97] Q. Li, Y. L. He, Y. Wang, and W. Q. Tao, Phys. Rev. E **76**, 056705 (2007).